Chapter 5

5.1 Introduction

In this chapter, we have discussed the structural transformation in $GdMnO_3$ perovskite after doping Cr^{3+} ion. Structural analysis of these perovskites are elaborated in section 5.2.1 using XRD. The reduction in J-T is discussed through Raman and Photoluminesence properties in section 5.2.2 and 5.2.3, respectively. Section 5.3 describes the magnetic properties. Conclusions of this chapter are discussed in section 5.4.

5.2 Structural and Optical Analysis

The structural transformation of Cr doped samples is discussed using the Rietveld refinement of the XRD patterns. The reason behind the structural transformation i.e J-T distortion is also discussed using XRD, Raman and photoluminescence spectroscopy in section 5.2.1, 5.2.2 and 5.2.3, respectively.

5.2.1 X-ray diffraction; Rietveld refinement and J-T distortion

Figure 5.1 illustrates the room temperature XRD patterns along with Rietveld refinement of $GdMn_{1-x}Cr_xO_3$ (x=0.1, 0.2, 0.3 and 0.4). XRD data refined over $2\Theta=20\text{-}80^o$ having *O*' type distorted perovskite structure, space group, *Pbnm*, upto x=0.3 as evidenced from the Bragg's positions indicated by green bars. Thus, $GdMn_{1-x}Cr_xO_3$ crystallizes as a single phase without any trace of impurity phase. Interestingly, with increasing concentration of Cr from 0.3 to 0.4, *O*' orthorhombic structure transforms into *O* type one. In our recent work, we have demonstrated structural transformation from *O*' orthorhombic to *O* type orthorhombic one by varying concentration of Fe from 30 to 50 at% in $GdMnO_3$

[105]. Due to orthorhombic structure, we have expressed the lattice parameters as a ≈ b ≈ c/√2. For a< c/√2<b, the perovskite adopts *O* type orthorhombic structure whereas the condition i.e. c/√2<a<b satisfies the *O'* orthorhombic structure.

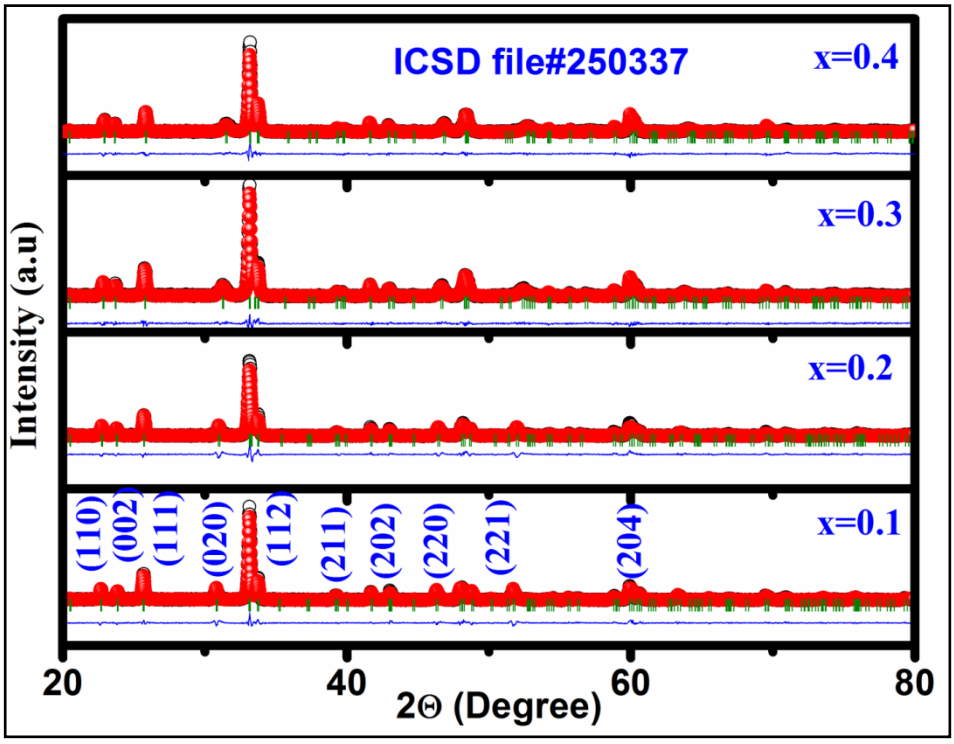

Figure 5.1 *Rietveld refinement of X-ray diffraction (XRD) patterns of* $GdMn_{1-x}Cr_xO_3$ *(x=0.1, 0.2, 0.3 and 0.4).*

After Rietveld refinement, the obtained parameters are tabulated in Table 1. Following the fitting parameters, the Rietveld refinement appears to be fairly satisfactory looking at the difference plot shown as blue line and the small value of χ^2. The change in lattice parameters with composition of Cr is shown in **figure 5.2**. One may notice from **figure 5.2** that with increasing Cr concentration while a and b decreases, c increases with reduction in lattice volume from 231.22 to 228.20 $Å^3$ with increasing Cr from 0.1 to 0.4. The significant

decrease in lattice volume is attributed to the difference in ionic radii of Cr and Mn ions**.** The smaller ionic radius of Cr^{3+} (0.61 Å) than that of Mn^{3+} (0.64 Å) shows a noticeable decrease in lattice volume confirming the substitution of Cr^{3+} ions at Mn^{3+} site in the lattice.

Table 5.1 Structural Parameters of $GdMn_{1-x}Cr_xO_3$ (x= 0.1, 0.2, 0.3 and 0.4) at room temperature revealed from the structure refinement.

Parameters	**x=0.1**	**x= 0.2**	**x= 0.3**	**x=0.4**
Gd(x, y, z)	(0.9833(6), 0.0806(4),0.25)	(0.9840(7), 0.0768(5),0.25)	(0.9850(5), 0.0720(3), 0.25)	(0.9807(5), 0.691, 0.25)
Mn/Cr (x, y, z)	0.5,0,0	(0.5,0,0)	(0.5,0,0)	(0.5,0,0)
O1 (x, y, z)	(0.095(3), 0.492(3),0.25)	(0.096(4), 0.475(4),0.25)	(0.1137(3), 0.4649(3),0.25)	0.087(4), 0.450(4), 0.25
O2 (x, y, z)	(0.703(3), 0.303(3), 0.0437(19))	(0.705(4), 0.298(4), 0.047(2)	(0.7788(3), 0.8215(3), 0.0495(3)	0.697(3), 0.306(3), 0.035(2)
χ^2	1.33	2.12	2.77	2.30
Mn-O1(Å)	1.93	1.944(6)	1.982(9)	1.958(6)
Mn-O2 (Å)(l)	2.24	2.07(2)	2.214(14)	2.046(17)
Mn-O2' (Å)(s)	1.87	1.99(2)	1.901(7)	1.968(16)
Mn-O1-Mn(deg)	148	148.4	142.53(12)	147.8(2)
Mn-O2-Mn(deg)	147.5	151.1(9)	148.86(11)	151.2(7)
|a-b|	0.4896	0.4594	0.4089	0.3685
σ_{JT}	0.066	0.053	0.046	0.037

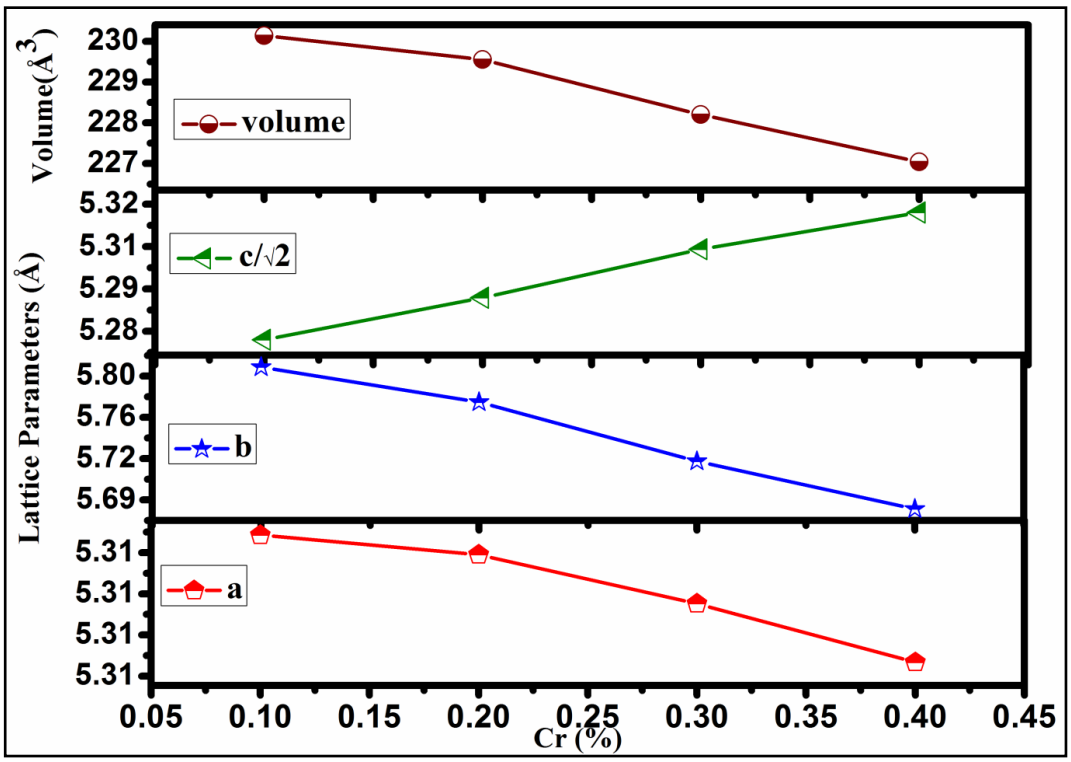

Figure 5.2 *Variations in lattice parameters and volume with Cr concentration.*

Further, on the basis of parameters obtained from Rietveld refinement, we show a representative unit cell of the crystal structure in three dimension (3D) indicating MnO_6 octahedra with spatial orientations and atom positions using Vista software depicted in **figure 5.3** for x=0.3 and 0.4. In MnO_6 octahedra, O1 atoms (red balls) reside at the two apical positions whereas O2 atoms (green balls) occupy four equatorial positions. The equatorial Mn-O2 bonds have two distinct bond lengths indicated as long (*l*) and short (*s)*. If all of the Mn-O and average <Mn-O> bond lengths are calculated from XRD patterns, the coherent J-T distortion is estimated by following expression.

$$\sigma_{JT}^2=1/3\Sigma_i[(Mn\text{-}O)_i\text{-}<Mn\text{-}O>]^2 \qquad (1)$$

The estimated values of σ_{JT} tabulated in **Table 5.1**. For $GdMnO_3$, there exists a large J-T distortion factor i.e. σ_{JT} = 0.2 [105]. However, after incorporating Cr into the host lattice,

σ_{JT} is found to be ~0.066 which reduces to 0.053 and 0.046 with increasing the Cr concentration from 0.1 to 0.2 and 0.3**,** respectively.

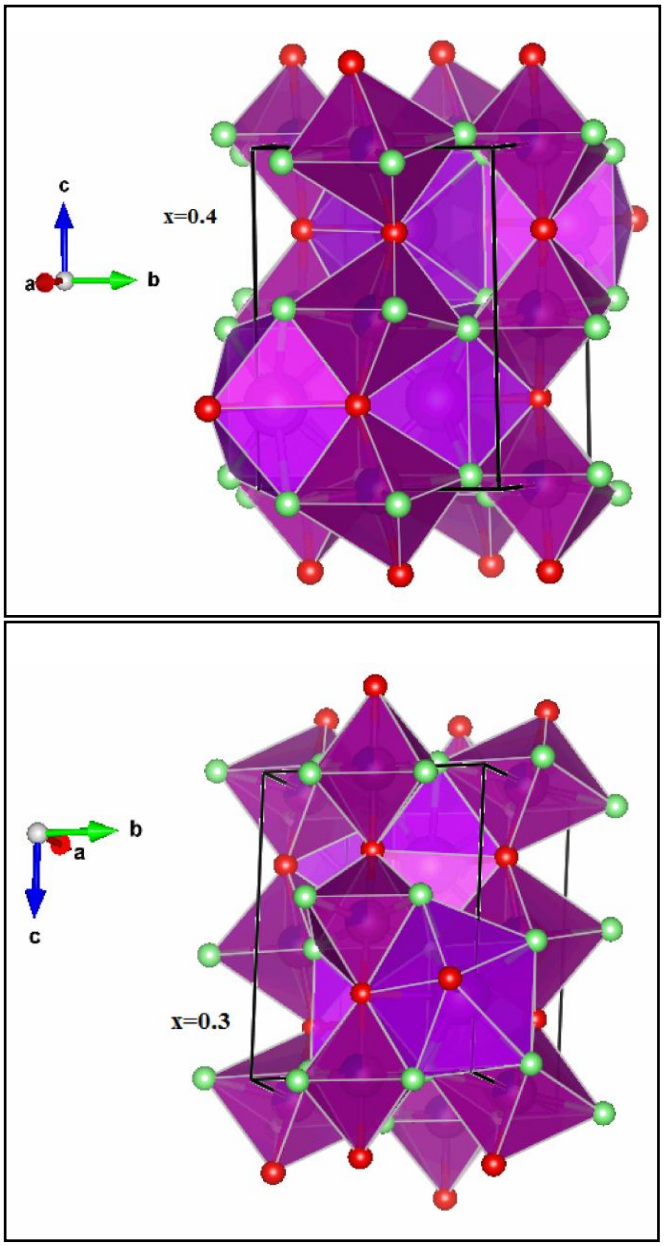

Figure 5.3 *Crystal structure obtained from Rietveld refinement drawn using Vesta software.*

For x=0.4, where *O'* to *O* orthorhombic structural transformation takes place, J-T distortion reduces to 0.037 which is almost 50% of the J-T factor observed in case of x=0.1. The considerable reduction in J-T distortion factor is ascribed to the replacement of J-T active element Mn^{3+} ions by the non-J-T active, Cr^{3+} ions in the lattice. Further, the reduction in the difference of lattice parameters (|a-b|) with increasing Cr reveals crystal structure with higher symmetry i.e. tetragonal unit cell.

5.2.2 Raman Spectroscopy

To confirm the change in J-T distortion with increasing Cr concentration, we have undertaken of Raman spectroscopic measurement. Raman spectra of $GdMn_{1-x}Cr_xO_3$ (x= 0.1, 0.2, 0.3 and 0.4) at room temperature are shown in **figure 5.4**. In case of x=0.1, the spectrum exhibits a tilting mode at 365 cm^{-1} along with the two J-T stretching modes i.e. anti-stretching (*as*) mode, A_{1g} at 474 cm^{-1} and stretching (*s*) mode, B_{2g} at 608 cm^{-1} in Fig.2 [106]. A_{1g} and B_{2g} modes arise due to in-plane antisymmetric vibration and stretching of O2, respectively which are correlated with J-T distortion. With increasing concentration of Cr from 0.2 to 0.3, both A_{1g} and B_{2g} are found to be red-shifted indicating smaller Mn—O bond length (d_{Mn-O}) keeping the intensity of peaks almost same. Apparently, at x=0.4, the drastic suppression of these peaks demonstrate further the structural transformation from *O*' to *O* type orthorhombic leading to significant decrease in J-T distortion. The fingerprint of J-T distortion induced structural transformation in Cr doped $GdMnO_3$ is investigated further through photoluminescence studies.

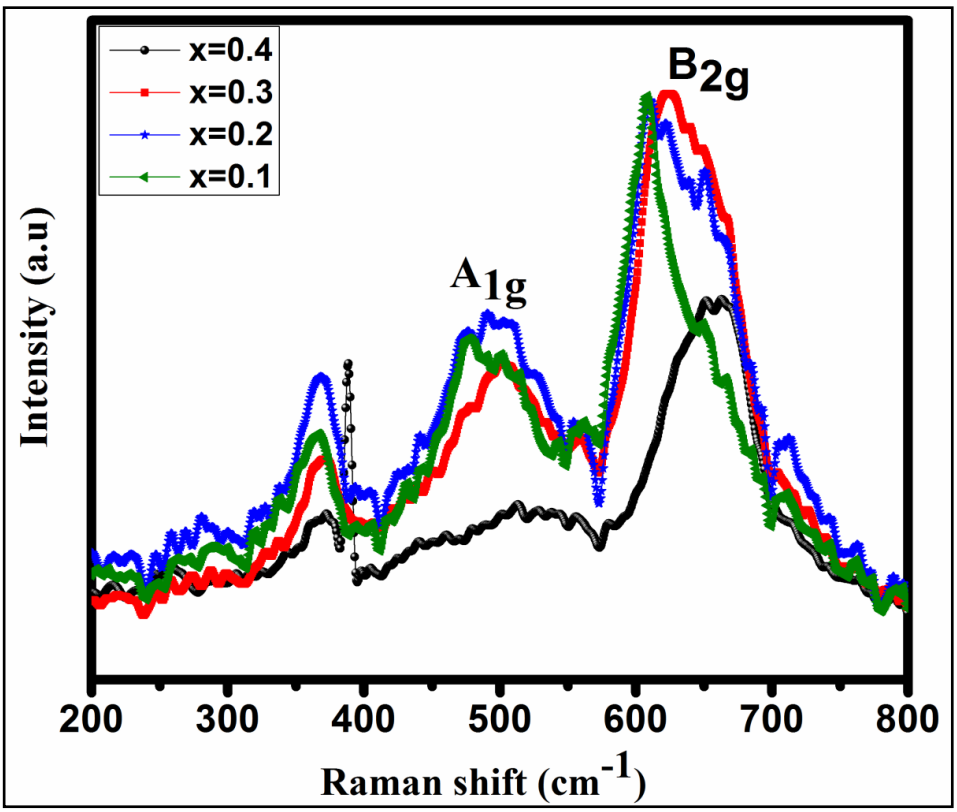

Figure 5.4 *Raman spectra of* $GdMn_{1-x}Cr_xO_3$ *(x= 0.1, 0.2, 0.3 and 0.4).*

5.2.3 Photoluminescence Properties

Figure 5.5 depicts the emission spectra of $GdMn_{1-x}Cr_xO_3$ (x=0, 0.3 and 0.4) after exciting with 200 nm. The spectra consist of broad emission peaks in wavelength range of 270-370 nm. For a simplified comparative analysis, we have deconvoluted the emission spectra to reveal dominant emission peaks. The emission spectrum of pure $GdMnO_3$ shows four distinct peaks at ~286, 308, 336 and 353 nm. In case of large J-T distortion, it is known that Mn^{3+} exhibits four distinct energy levels at 3.5, 4, 8 and 8.5 eV corresponding to transition from O2*p* to Mn(t_{2g}−JT), Mn(t_{2g} + JT), Mn(e_g−JT), Mn(e_g + JT), respectively [46]. The emission peak at ~286 can be assigned to O2*p* → Mn(t_{2g} + JT) transition of Mn^{3+}. The peak at 308 nm is attributed to the band transition, $^4T_{1g} \rightarrow {}^4A_{2g}$ of Mn^{4+}. Owing to

broad nature of this peak, the energy level Mn(t_{2g} - JT) of Mn^{3+} having comparable energy to Mn^{4+} can also contribute towards this emission. The other peak located at 336 nm while emerges from relaxation of electrons from $^4T_{1g}$ energy band to $^4A_{2g}$, peak at 353 nm originates from the electronic transition, $^2T_{2g} \rightarrow {}^4A_{2g}$, corresponding to Mn^{4+} [48]. After doping Cr (x=0.3 and 0.4), three peaks are found to be located at ~294, 332 and 355 nm. Surprisingly, the emission peak at ~286 nm observed in $GdMnO_3$ disappears completely by incorporating Cr in host lattice.

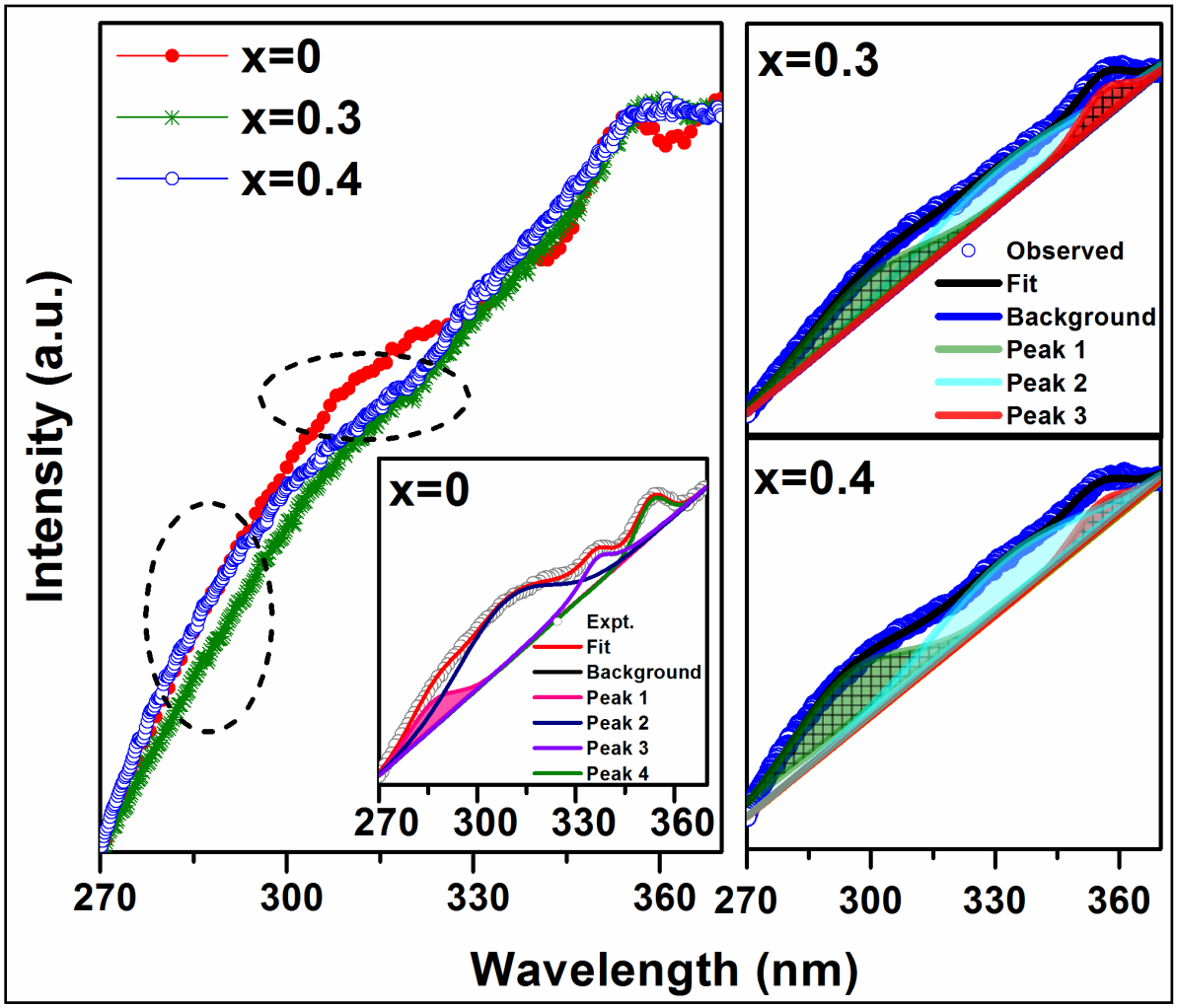

Figure 5.5 *The emission spectra of $GdMn_{1-x}Cr_xO_3$ (x=0, 0.3 and 0.4) under the excitation wavelength of 200 nm. (Inset depicts the deconvoluted peaks).*

The disappearance of above peak could be due to the J-T distortion factor of 0.2 observed in $GdMnO_3$ which reduces to 0.046 and 0.037 in x=0.3 and 0.4, respectively. Under reduced J-T distortion, the energy gap between Mn(t_{2g} − JT) and Mn(t_{2g} + JT) reduces significantly. Considering this fact, the broad emission peak at ~294 nm arises mainly from $^4T_{1g} \rightarrow {}^4A_{2g}$ of Mn^{4+} whereas other peaks at ~332 and 355 nm remain same. In this context, in our previous work, we have also shown the disappearance of peak at ~286 nm after doping Fe in $GdMnO_3$ where J-T distortion has been reduced by one order magnitude [[105]]. Moreira et al. have also mentioned the disappearance of PL emission peak in $CaTiO_3$ due to undistorted or ordered TiO_6 clusters [100]. J-T distortion factor less by one order magnitude thus influences the PL spectra in Cr doped $GdMnO_3$.

Figure 5.6 shows the emission spectra of $GdMn_{1-x}Cr_xO_3$ (x=0-0.4) under an excitation wavelength of 460, 582 and 625 nm. After exciting at wavelength of 460 nm, the emission spectrum of $GdMnO_3$ exhibits a broad peak ranging from 675-720 nm centered at ~692 nm lying in red region. This emission peak is attributed to the spin-forbidden, $^2E_g \rightarrow {}^4A_{2g}$ transition of Mn^{4+} ion. Since Mn^{4+} exhibits large effective positive charge, this transition is found to be dominated in the emission spectrum due to strong crystal field of the host [48]. After incorporating Cr into $GdMnO_3$, although the intensity of emission peak at ~692 nm changes significantly, no change in peak position is observed. Exciting $GdMnO_3$ with 582 nm, one broad emission having a maximum at 645 nm is observed indicating a blue-shift of ~45 nm. Under an excitation wavelength of 625 nm, for $GdMnO_3$, the broadband emission peak is found to be located at ~690 nm. In case of x=0-0.2, the intensity of peak is nearly same which diminishes for x= 0.3 and 0.4. The peak position of emission i.e. ~692 nm of Mn^{4+} can vary significantly depending on the host material and

excitation wavelength. For example, while this peak is observed at ~617 nm in Na_2SiF_6, same peak is found to be red shifted by ~100 nm showing prominent emission at 723 nm in $SrTiO_3$ [107].

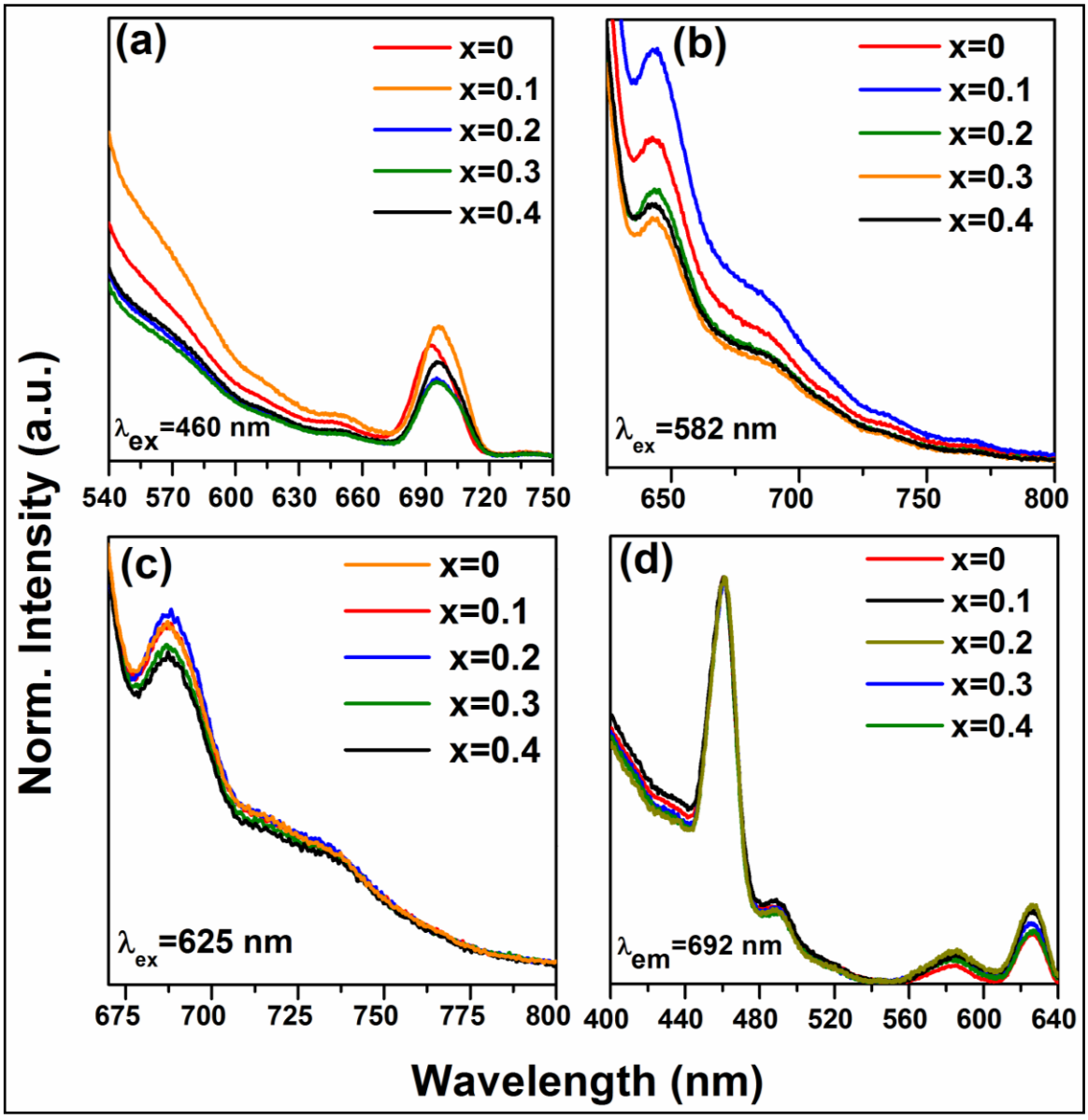

Figure 5.6 *The emission spectra of $GdMn_{1-x}Cr_xO_3$ (x=0, 0.1, 0.2, 0.3 and 0.4) at (a) λ_{ex}= 460 nm, (b) λ_{ex}= 582 nm, (c) λ_{ex}= 625 nm and (d) the excitation spectra after monitoring λ_{em}= 692 nm.*

The excitation spectra have been taken by monitoring λ_{em}=692 nm depicted in **figure 5.6.** In $GdMnO_3$, the excitation spectrum is comprised of a strong peak at ~460 nm along with a shoulder peak at ~490 nm. This excitation peak is primarily attributed to $^4A_{2g} \rightarrow {}^2T_{2g}$ electronic transition of Mn^{4+} ion in the lattice. Two more sharp peaks are observed to be centered at ~582 and ~625 nm. The former one originates because of $^4A_{2g} \rightarrow {}^4T_{2g}$ transitions whereas the latter one is ascribed to the local vibration-activated $^2E_g \leftrightarrow {}^4A_{2g}$ transitions of Mn^{4+} ion [107]. We do not observe any change in the intensity of peak at ~460 nm with increasing Cr concentration. However, one can see an appreciable enhancement in the intensity of excitation peaks at ~582 and 625 nm for x=0.1 and 0.2

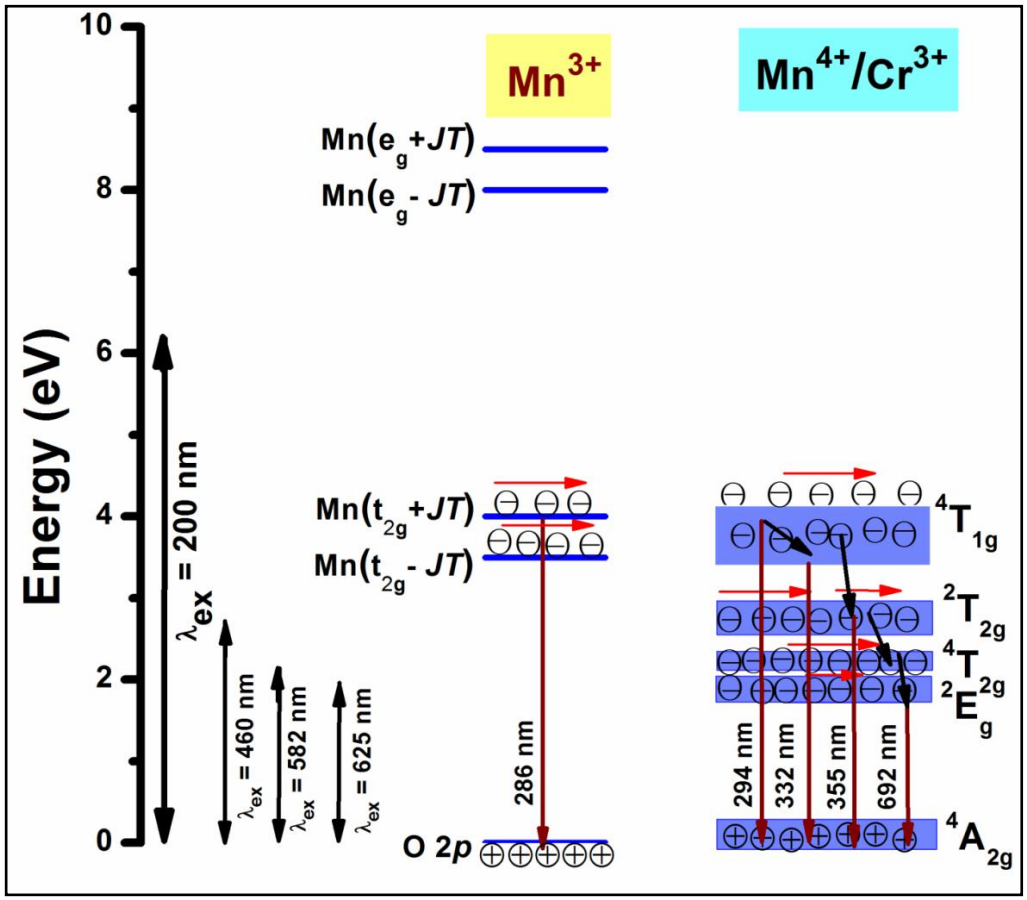

Figure 5.7 *The proposed energy band diagram for Cr doped $GdMnO_3$.*

which reduces when x=0.3 and 0.4. It is known that energy bands of Cr^{3+} are almost similar to Mn^{4+} which may result into overlapping of different energy bands. Therefore, we have proposed an energy band diagram (**figure 5.7*)*** to explain the luminescence behavior of $GdMn_{1-x}Cr_xO_3$ showing various energy levels such as O*2p*, Mn(t_{2g}− JT), Mn(t_{2g} + JT), Mn(e_g−JT), Mn(e_g + JT) of Mn^{3+} under J-T effect, ^2E_g, $^4T_{2g}$, $^2T_{2g}$, $^4T_{1g}$, $^4A_{2g}$ associated to Mn^{4+} and Cr^{3+} ion, respectively. After exciting with 200 nm, the excited electrons do not reach to Mn(e_g− JT) and Mn(e_g + JT) of Mn^{3+} due to large energy gap. However, the energetic electrons are only transferred to Mn(t_{2g}−JT) and Mn(t_{2g} + JT) which relax to O2*p* showing emissions at 286, 294/308, 332 and 355 nm. After exciting with 460 nm, the electrons are not excited to t_{2g} of Mn^{3+} or $^4T_{1g}$ of Mn^{4+}/Cr^{3+} due to significant energy gap. In pure $GdMnO_3$, the excited electrons reach at $^2T_{2g}$ of Mn^{4+} which follow multistep relaxation via $^4T_{2g}$ to ^2E_g and eventually come back to $^4A_{2g}$ inducing strong emission peak at ~692 nm. In the presence of Cr^{3+} ion, the similar energy levels of Cr^{3+} and Mn^{4+} can influence the intensity of this emission peak by providing additional energetic electrons. Under excitation with higher wavelength of 582 nm, the excited electrons residing at $^4T_{2g}$ of Mn^{4+}/Cr^{3+} de-excited to ^2E_g and finally relax to $^4A_{2g}$ showing a similar emission band at ~645 nm. However, at λ_{ex}=625 nm, this emission band arises due to absorption/emission process occurring between $^4A_{2g}$ and ^2E_g energy levels. Thus, it is established that in Cr doped $GdMnO_3$, the photoluminescence properties of Mn^{4+} can be modified by Cr^{3+} ion due to the presence of additional energetic electrons providing improved emissions in red region under different excitation wavelengths.

5.3 Magnetic Properties

To study the magnetic properties after Cr doping upto 40 at%, the temperature dependent magnetization, magnetic field dependent magnetization and time dependent magnetization and magnetic switching are carried out.

5.3.1 Temperature dependent magnetization

Figure 5.8 depicts the temperature dependent magnetization (M vs. T) under the applied magnetic field of 500 Oe for $GdMn_{1-x}Cr_xO_3$ (x= 0.1- 0.4). With decreasing temperature from 300 K, below T_N, M_{ZFC} and M_{FC} bifurcates at ~31 K for x= 0.1. Further, decreasing temperature, while M_{ZFC} increases and attains the maximum magnetization at temperature T_P, which is broad in nature, M_{FC} increases continuously. In the case of x= 0.2, however, after bifurcation of M_{ZFC} and M_{FC} at ~ 63 K, M_{ZFC} crosses over the M_{FC} at temperature ~31 K, indicating a magnetic phase transition. Upon reducing temperature further, M_{ZFC} attains maxima (~2.2 emu/g) at T_P ~19 K, whereas M_{FC} increases continuously. For x= 0.3, although bifurcation is observed at ~95 K, T_P remains same as in case of x=0.2 except a decrease in M_{max} to ~1.56 emu/g.

On the other hand, M_{FC} in the case of x=0.3 shows a maximum of 0.45 emu/g at T_{max} ~36 K followed by decrease in magnetization attaining a minimum value of ~0.32 emu/g at ~28 K. The temperature at which minimum magnetization observed is known to be spin-reorientation temperature (T_{SR}). Although $T_{SR,}$ is not detectable from ZFC and FC plot in x=0.2, it is observed at ~25 K by plotting $(M_{ZFC}-M_{FC})/M_{ZFC}$ vs T (**figure 5.9**). In case of x= 0.4, after bifurcation of M_{ZFC} and M_{FC} at ~ 110 K, M_{ZFC} attains a maxima of 0.71 emu/g at ~ 19 K same as the T_P of x=0.2. Besides, with decreasing temperature, M_{FC} increases showing a M_{max} ~1 emu/g at ~ 42 K and further decreasing temperature, M_{FC}

crosses the temperature axis (T=0) at ~27 K, known to be compensation temperature, T_{comp}. Below T_{comp}, the M_{FC} becomes negative and attains a minimum magnetization, -5.83 emu/g, at temperature ~ 2 K. It is important to note that when x is 0.4, an interesting property of magnetization reversal is observed with applying magnetic field of 500 Oe. Further, decreasing the applied magnetic field to 50 and 100 Oe, we could observe the magnetization reversal in x=0.3 as well which is absent under an applied field of 500 Oe.

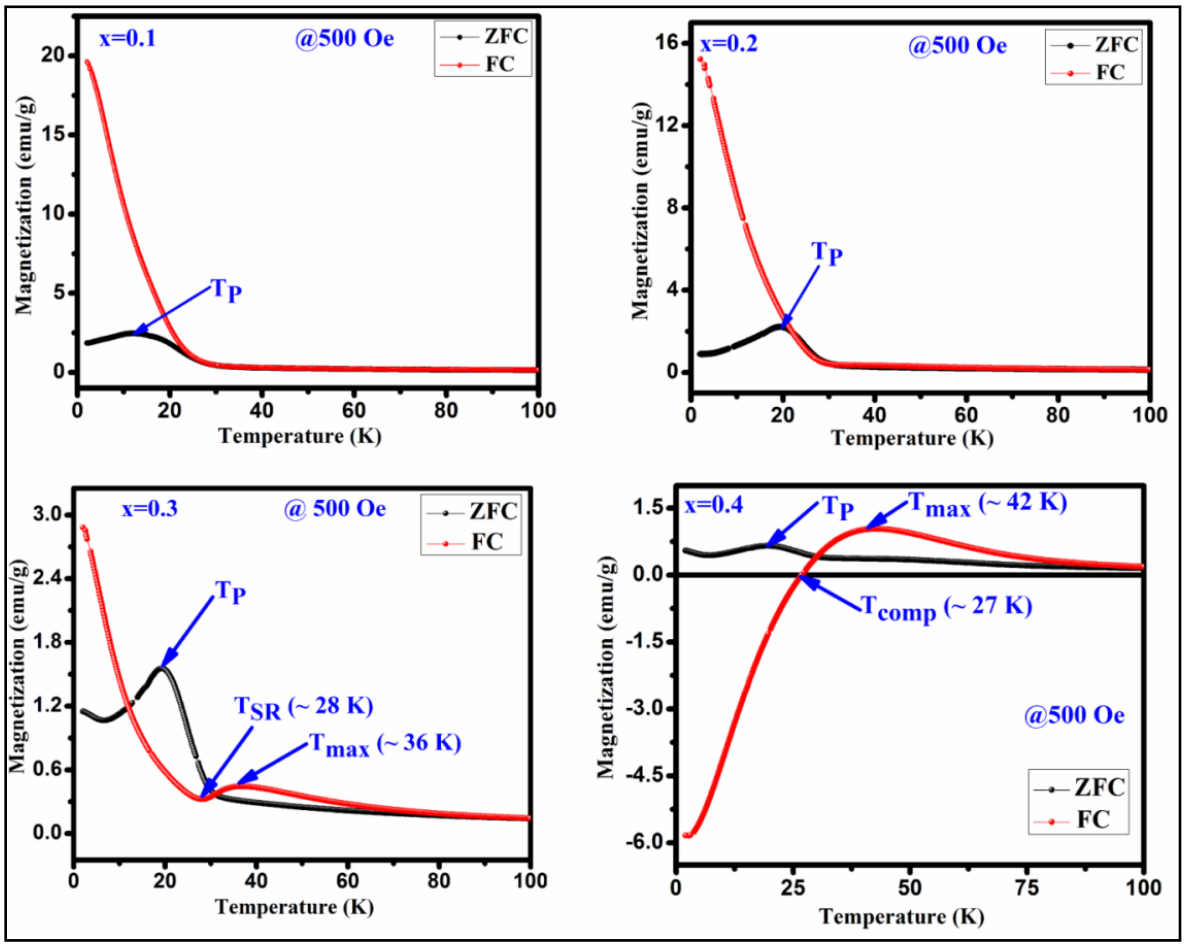

Figure 5.8 *Temperature dependent magnetization under zero field cooling (ZFC) and field cooling (FC) measured at 500 for* $GdMn_{1-x}Cr_xO_3$ *(x=0.1- 0.4).*

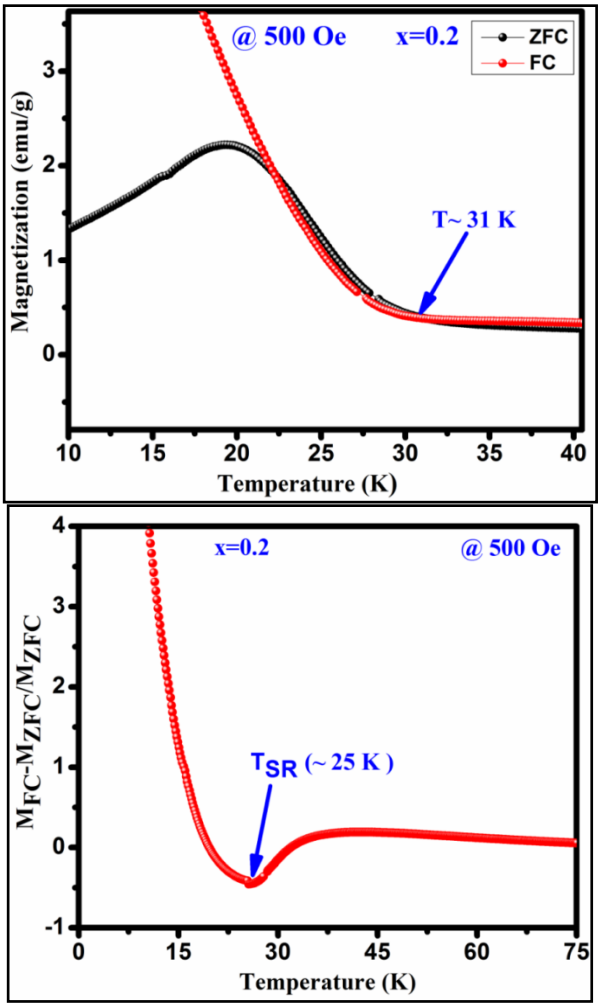

Figure 5.9 *Zoom part of Temperature dependent magnetization under zero (ZFC) and field cooling (FC) measured at 500 Oe and* $(M_{ZFC}-M_{FC})/M_{ZFC}$ *vs T for* $GdMn_{1-x}Cr_xO_3$ *(x= 0.3).*

Moreover, except at x=0.1**,** we show that with increase in Cr concentration upto 0.4, one can observe T_{SR} and T_{comp} with varying the applied field from 50 to 500 Oe. The mechanism of the magnetization reversal can be understood in terms of negative exchange interaction between two component**s** such as Cr and Gd ions. The ferromagnetic order emerging due to canted AFM ordering of Cr^{3+} produces an internal field at paramagnetically ordered Gd^{3+} ions which are aligned to that of net Cr^{3+} moment**.** When external field is applied, the component of Cr^{3+} (M_{Cr}) is pointed along the external field

direction while Gd^{3+} ion experiencing the internal field opposite to that of external field. Therefore, the net magnetization of the system, $M_s = M_{Cr} - M_{Gd}$ varies with temperature and external field. In the region $T>T_{comp}$, the M_{Cr} dominates over M_{Gd} resulting into a net positive magnetization in field direction giving a maxima in M_{FC} (shown in **figure 5.10**). At a critical temperature magnetization corresponding to M_{Gd} and M_{Cr} cancel out**,** resulting a zero magnetization known as T_{comp}. Decreasing the temperature further the magnetization becomes negative as the moment of Gd^{3+} ion is increased while $M_{Cr}{}^{3+}$ remains the same. As a consequence, $M_{Gd}{}^{3+}$ dominates over the magnetization corresponding to $M_{Cr}{}^{3+}$.

A typical M_{FC} magnetization vs temperature plot of Cr^{3+} and Gd^{3+} under 50 Oe at $T>T_{comp}$ and $T<T_{comp}$ is shown in **figure 5.10**. While with applying low field, we could observe a magnetization maxima in FC curve and magnetization reversal followed by spin reorientation transition, with application of high field (500 Oe), the rotation of moment of $M_{Gd}{}^{3+}$ ion takes place along the external field direction since the applied field is large enough to overcome the internal field generates by Cr^{3+} ions. Hence a positive magnetization is observed in whole temperature range. With varying Cr concentration, the applied field strength also changes which essentially evokes a positive magnetization in FC mode. For instance, in x=0.1 and x=0.2, the magnetization is always positive independent of applied field. However, in x=0.3 while the FC magnetization is positive under 500 Oe, we do not observe positive magnetization upto 500 Oe for x=0.4 (**figure 5.11**). Magnetization reversal has been reported in orthochromites, orthoferrites and orthovanadates [108-110]. The T_{SR} is also observed at ~ 4.8 K from $(M_{ZFC}-M_{FC})/M_{ZFC}$ plot as in case of x=0.3. The presence of T_{SR} could be ascribed to the interactions between different ion pairs such as $Gd^{3+} - Gd^{3+}$ and $Gd^{3+} - Mn^{3+}$.

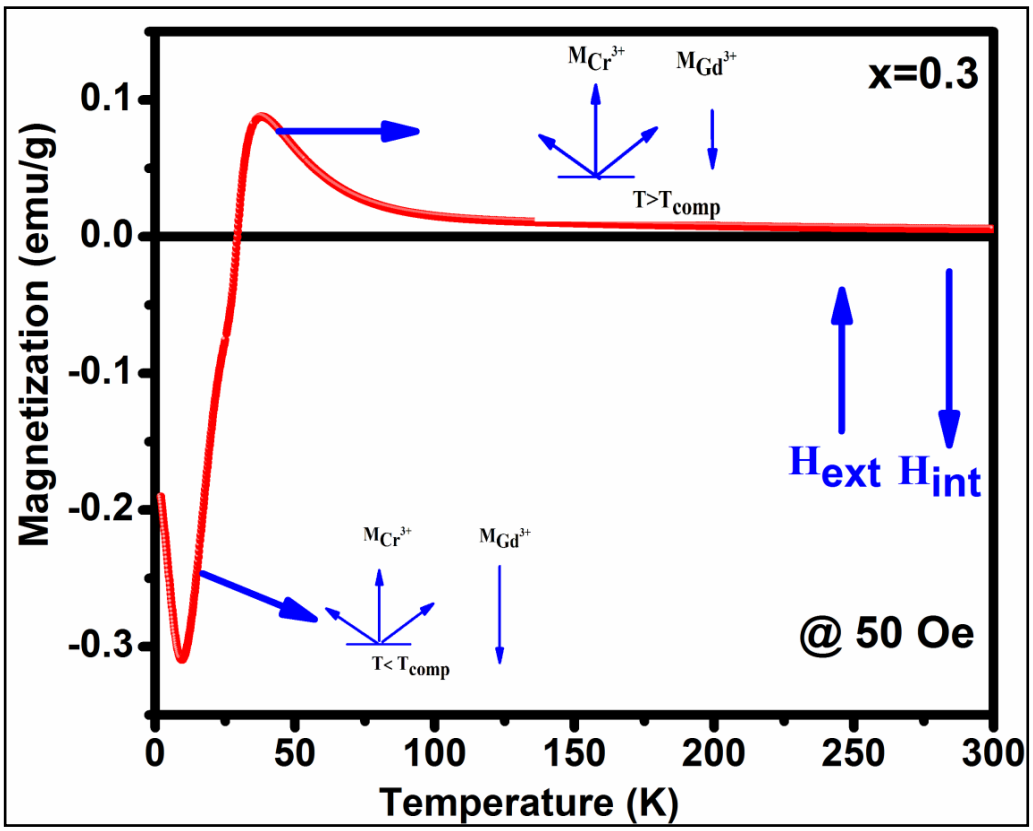

Figure 5.10 *Schematic diagrams of the Cr^{3+} moment (M_{Cr}) and Gd^{3+} moments under different temperature range.*

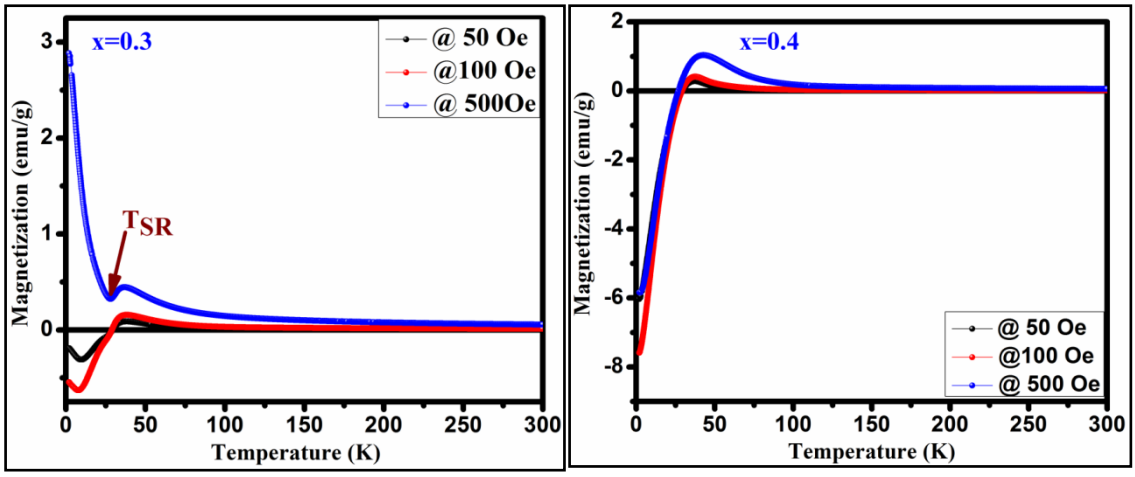

Figure 5.11 *Temperature dependent magnetization under field cooling (FC) measured at different fields for $GdMn_{1-x}Cr_xO_3$ (x= 0.3 and 0.4).*

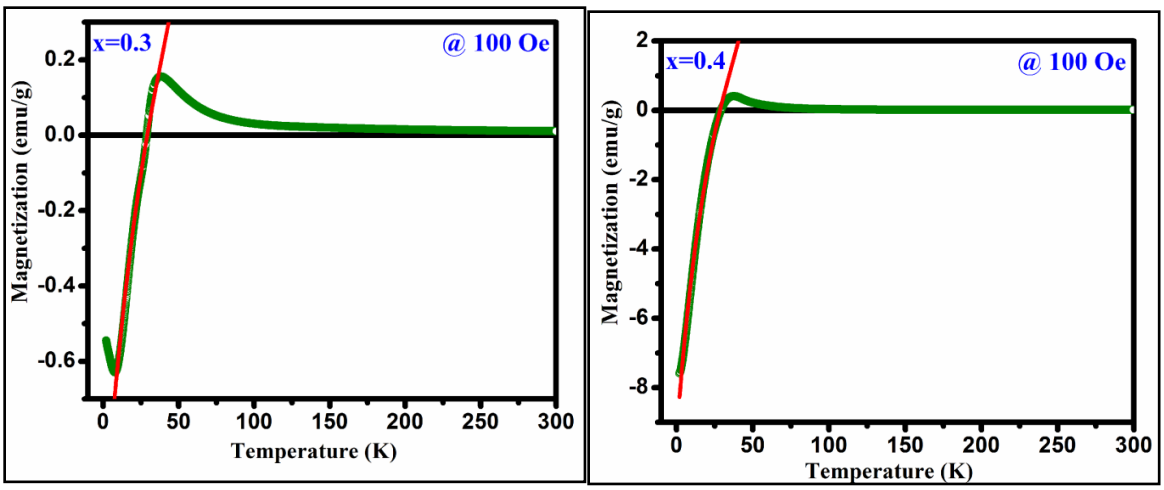

Figure 5.12 *Magnetization curves at 100 Oe applied field in FC mode (the red line shows fitting.*

The magnetization reversal has been further investigated by fitting the FC magnetization curves employing following equation:

$$\mathbf{M=M_{Cr}} + \frac{\boldsymbol{C(H+Hint)}}{\boldsymbol{T-\Theta}} \qquad (2)$$

where M, M_{Cr}, C, H, H_{int} and Θ is called as the total magnetization, magnetization due to the Cr^{3+} ions, Curie constant, applied magnetic field, internal magnetic field from Cr^{3+} ions, and Weiss temperature, respectively.

The fittings of M_{FC} at 100 Oe are shown in **figure 5.12** and the estimated parameters are tabulated in **Table 5.2** under the applied fields of 50, 100 and 500 Oe (figures are not shown). From **Table 5.2**, it is noteworthy to mention that H_{int} (due to Cr^{3+} ions) and the applied magnetic field (H) are in opposite direction to each other which changes with increasing H. The estimated enhancement in H_{int} and M_{Cr} values are attributed to the increase in strengthening of AFM ordering under an applied field [111]. Biswas *et al.* have also found same behavior in the case of $Gd_{0.7}Ca_{0.3}Mn_{1-x}Cr_xO_3$ (x= 0.0–0.5) [112]. Moreover, under low applied magnetic field, the canted Cr^{3+} and Gd^{3+} ions interact

antiferromagnetically giving rise to the negative value of Θ in the present system. Further, we have investigated the antiferromagnetic ordering of net magnetic moments applying external magnetic field below T_{comp}. Explicitly, a mirror-like behavior observed at ± 100 Oe for x= 0.3 and at ± 500 Oe for x= 0.4 is shown in **figure 5.13**.

Table 5.2 Fitting parameters for M-T curves recorded in the FC mode for .$GdMn_{1-x}Fe_xO_3$ (x= 0.3 and 0.4).

Composition	**External Field**	**M_{Cr} (emu/g)**	**H_I (Oe)**	**Θ**
x=0.3	50 Oe	0.98	-61.32	-51.24
	100 Oe	1.88	-121.50	-50.89
x=0.4	50 Oe	7.56	-188.42	-28.73
	100 Oe	11.40	-278.16	-34.54
	500 Oe	12.74	-642.79	-49.4

To determine the magnetic transition temperature, $1/\chi$ vs. temperature curves are plotted for $GdMn_{1-x}Cr_xO_3$ (x=0.1- 0.4) shown in **figure 5.14**. The antiferromagnetic Néel temperature (T_N) is found to be increased from ~49 and ~130 K when x is varied from 0.1 to 0.4. The estimated values are much higher than that of $GdMnO_3$ (i.e. T_N ~42 K) [105]. In addition, from $1/\chi$ vs. temperature plots, the effective magnetic moment (μ_{eff}) is calculated after fitting the data in paramagnetic region using Curie-Weiss law i.e. $1/\chi = (T-\Theta)/C$, where C is Curie constant and Θ is Curie-Weiss temperature (**figure 5.15**). The negative value of Θ indicates the antiferromagnetic coupling between the atoms in all samples. The μ_{eff} is estimated theoretically using the formula, $\mu_{eff} = [(\mu_{Gd})^2+(1-x)(\mu_{Mn})^2+x(\mu_{Cr})^2]^{1/2}$. The theoretical values of μ_{eff} are found to be 9.25, 9.20, 9.15 and 9.10 μ_B for x=0.1, 0.2, 0.3 and

0.4, respectively. The calculated theoretical and experimental moments do not show a significant difference.

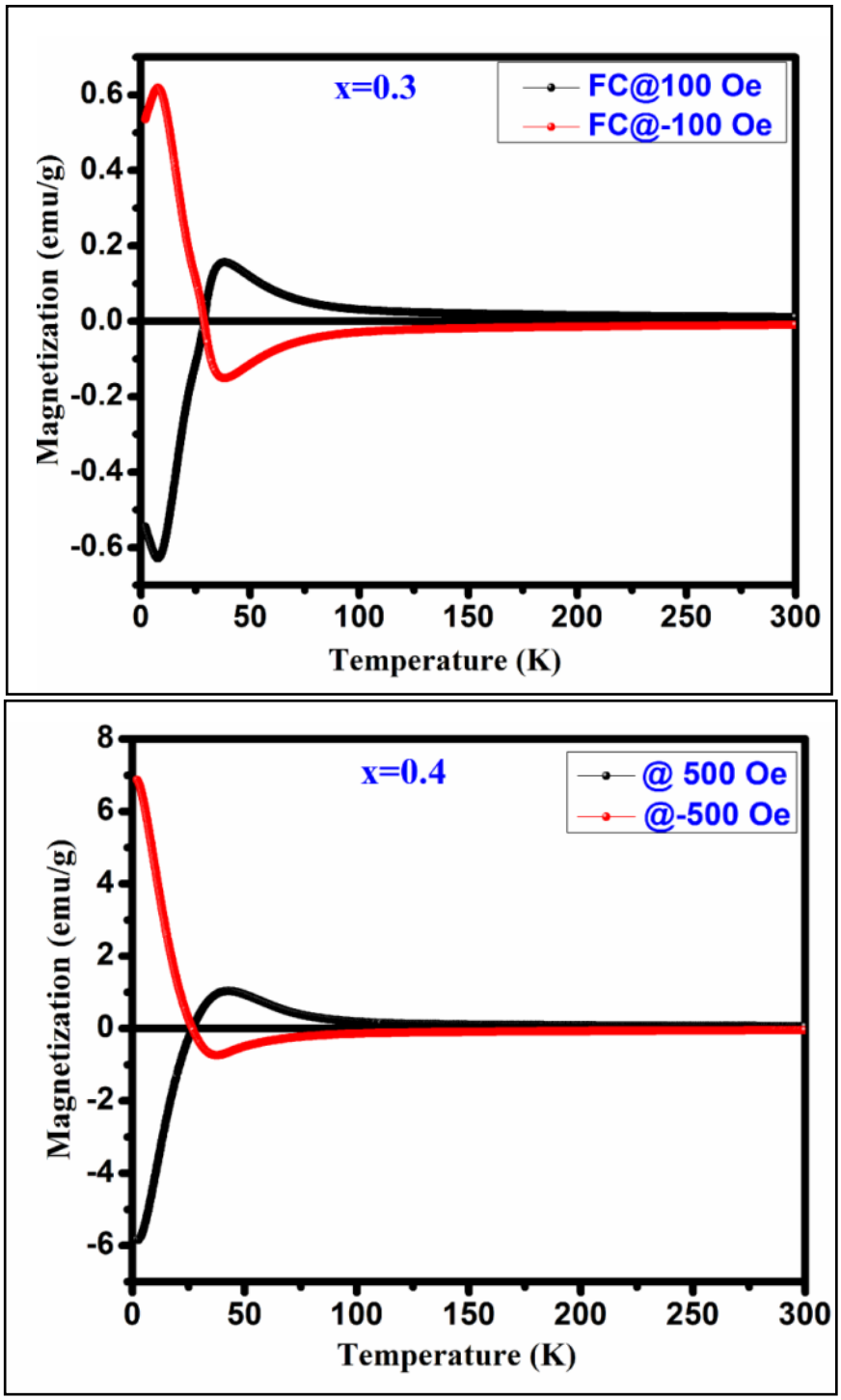

Figure 5.13 *Mirror like behavior in FC mode for* $GdMn_{1-x}Cr_xO_3$ *(x= 0.3 and 0.4).*

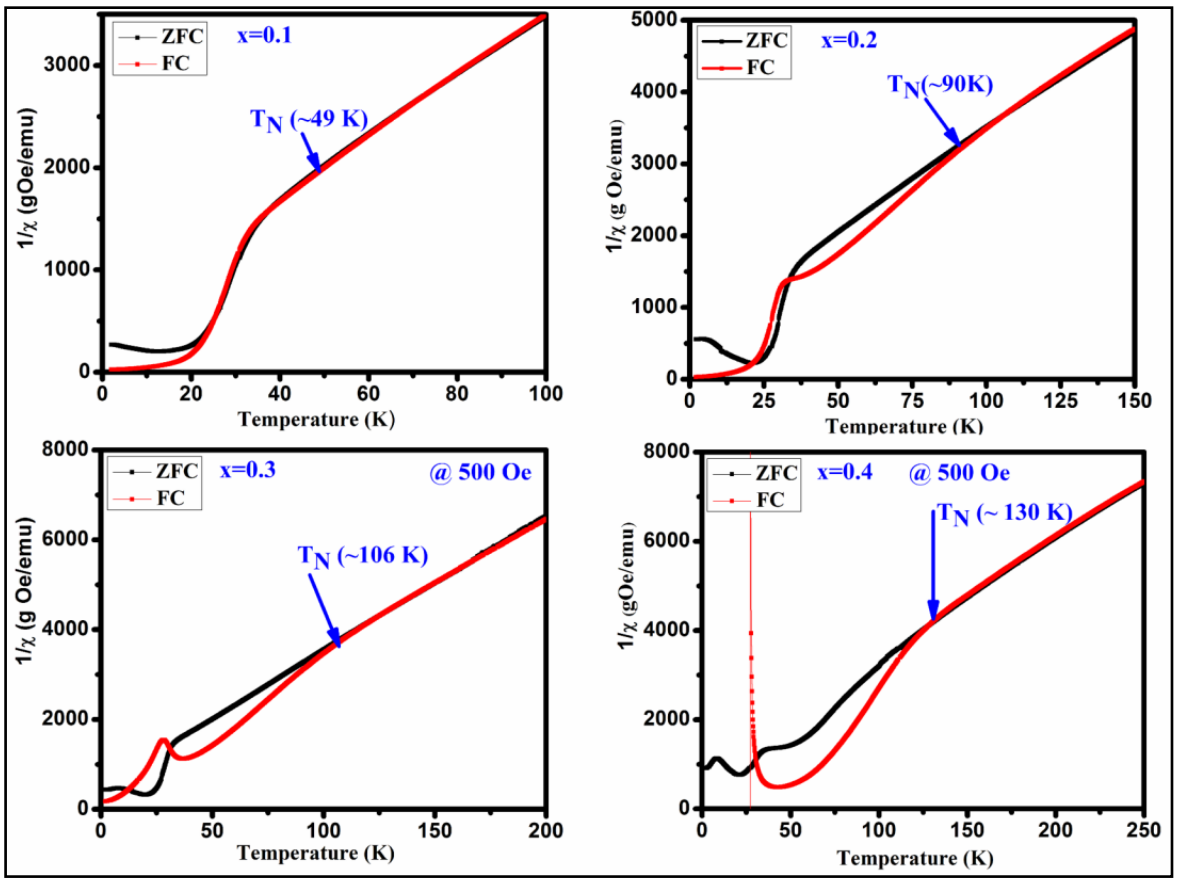

Figure 5.14 *The inverse susceptibility, $1/\chi$ plots of ZFC and FC in the presence of 500 Oe of the $GdMn_{1-x}Cr_xO_3$ (x= 0.1- 0.4).*

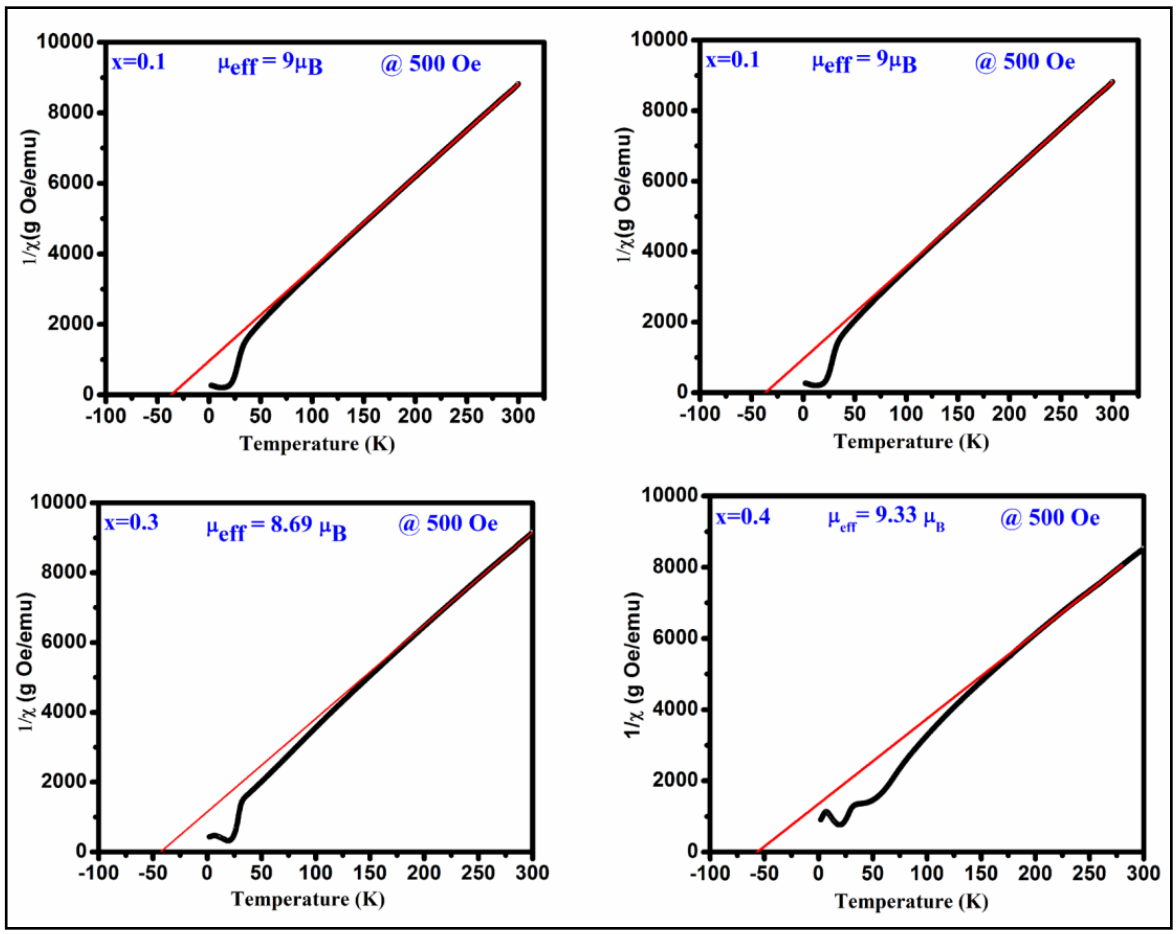

Figure 5.15 *Curie- Weiss law fitting in the presence of 500 Oe of the* $GdMn_{1-x}Cr_xO_3$ *(x= 0.1- 0.4).*

5.3.2 Magnetic field dependent magnetization

The magnetization (M) is recorded as a function of the external field (H) below T_N i.e. at 20 and 4 K for $GdMn_{1-x}Cr_xO_3$ (x=0.1-0.4) in ZFC mode shown in **figure 5.16**. At 20 K, the magnetization with a slim loop increases linearly with increasing field which does not saturate upto 70 kOe. Further, with decreasing the temperature to 4 K, the area under the loop enhances and the loops are symmetrical along magnetic and magnetization axes, indicate the absence of exchange bias. After analyzing the hysteresis loops measured at 4 and 20 K, the calculated values of maximum magnetization (M_{max}), coercivity (H_c) and

remanence (M_r) are given in ***Table 5.3***. Generally, the magnetization hysteresis loop and its linear increasing nature at high field appear due to the weak ferromagnetic ordering which primarily induced by deviation of the collinearity of the moments in an antiferromagnet. Mao *et. al.* discuss a similar behavior of magnetization as a function of external field in case of $YFe_{0.5}Cr_{0.5}O_3$ [113].

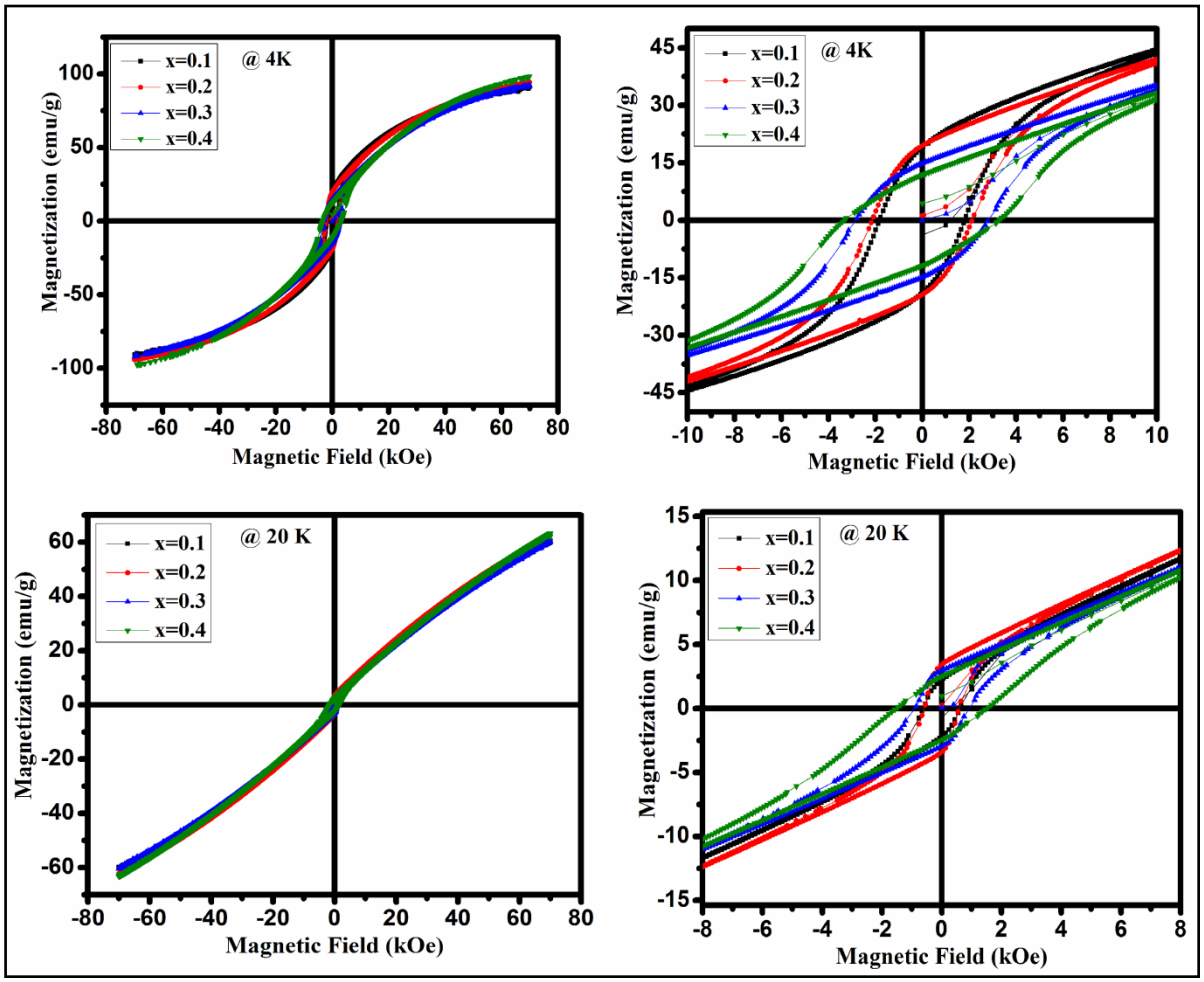

Figure 5.16 *Magnetic field dependent magnetization at 4 and 2 K of* $GdMn_{1-x}Cr_xO_3$ *(x= 0.1-0.4) with zoomed view.*

Table 5.3 Maximum magnetization (M_{max}), remenance (M_r) and coercivity (H_c) for $GdMn_{1-x}Cr_xO_3$ (x= 0.1, 0.2, 0.3 and 0.4) at 4 K and 20 K.

T (K) ↓	**M_{max} @ 7 kOe (emu/g)**				**H_C (Oe)**				**M_r (emu/g)**			
x →	**x= 0.1**	**x= 0.2**	**x= 0.3**	**x= 0.4**	**x= 0.1**	**x= 0.2**	**x= 0.3**	**x= 0.4**	**x= 0.1**	**x= 0.2**	**x= 0.3**	**x= 0.4**
4 K	90	95	92	98	1.81	2.16	2.83	3.23	19.3	19	14	12
20 K	60	63	60	63	0.62	0.59	0.92	1.56	2.2	3	3	2.3

5.3.3 Time dependent magnetization

The peak T_P observed in M vs. T measurements is a possible fingerprint of the presence of spin-glass (SG) behavior. The presence of SG behavior has been validated after analyzing the time dependent remanant magnetization measurements for x=0.1-0.4 shown in **figure 5.17**. This measurement is carried out by cooling sample from 300 to 15 K in under applied magnetic field of 100 Oe and then the field is removed. The magnetization is measured with varying time for 3 h. In general, the relaxation for SG behavior satisfies the power law, $M(t) = M_0 t^{-b}$ where M_0 i.e. M at t = 0 known as initial magnetization and b is the decay parameter [105]. It is clear from fitting of experimental data with above equation that the remanent magnetization satisfies the power law corroborating the SG like behavior in all samples.

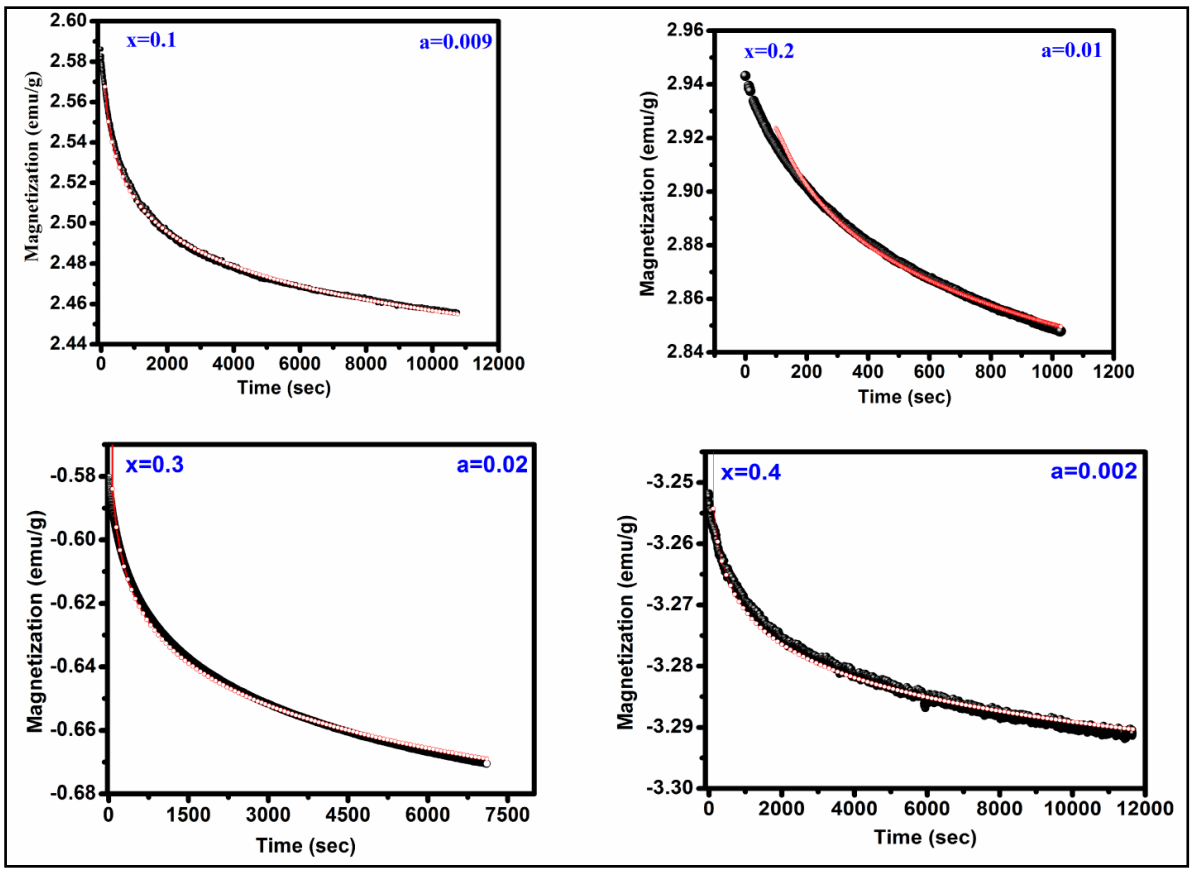

Figure 5.17 *Magnetic relaxation after field cooling in 100 Oe. The red line shows the fitting of experimental data with power law.*

5.3.4 Magnetic Switching

Owing to the existence of characteristic features like magnetic reversal, Cr doped $GdMnO_3$ (x=0.3 and x=0.4) has been explored for distinct magnetic switching effect. At 100 Oe, the sample is cooled down to 10 K in FC mode and magnetic switching measurements are recorded shown in Fig. 10. First, the magnetization is measured for 180 sec at 10 K. Then, the magnetic field is quickly increased to 500 Oe and 1700 for x=0.3 and 0.4, respectively followed by measuring the magnetization for constant time interval of 180 sec. Apparently, these samples exhibit a promising magnetic switching effect. The measurement cycles are repeated for several times to examine the switching reproducibility

which indicated reversible and continuous switching of the magnetization over cycles. The switching between the positive and negative magnetization states can be triggered through changing the magnitude of the field with fixed field direction. In this rise and decay time is 100 Oe/s. Moreover, this can be tuned in a predictable way. The magnetic switching effects driven by external magnetic field render promising application of these materials in magnetic data storage and magnetic switching based nonvolatile magnetic memory.

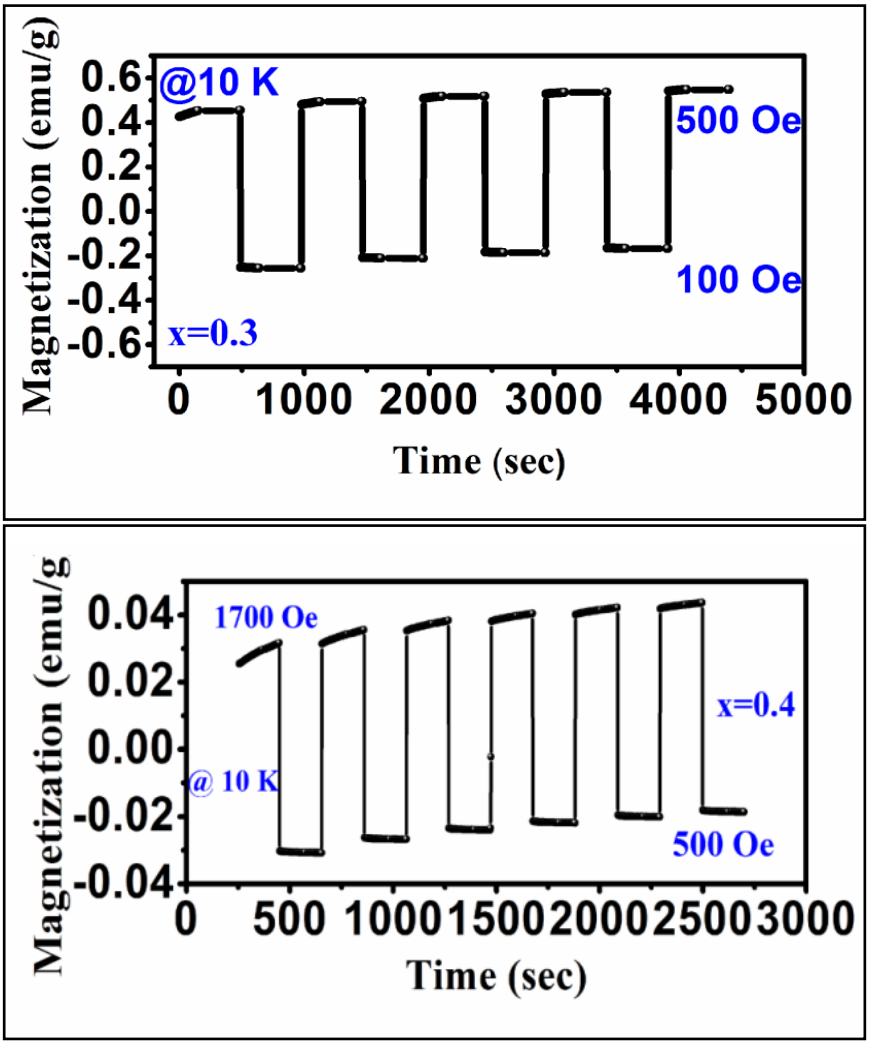

Figure 5.18 *Magnetic switching behavior of* $GdMn_{1-x}Cr_xO_3$ *(x= 0.3 and 0.4) at different field.*

5.4 Conclusions

In summary, we systematically examined the structural evolution and rich sequence of magnetic transitions in Cr doped $GdMnO_3$ synthesized using sol-gel technique. As Cr concentration is increased from 0.1 to 0.4, we observed the structural transformation from *O'* to *O* type orthorhombic one along with the reduction in lattice volume. The decrease in lattice volume was due to the smaller ionic radius of Cr^{3+} compared to Mn^{3+}. The structural transformation was manifested by the reduction in J-T distortion factor calculated using the bond length obtained from Rietveld refinement. Raman spectra supported the observed reduction in J-T distortion factor as reflected showing decrease in the intensity of asymmetric stretching bonds at 487 and 610 cm^{-1}. Further, the emission peak at ~286 nm in PL spectra disappeared indicating decrease in J-T distortion factor. PL study demonstrated the emission spectra related to Mn^{4+} energy levels which improved after incorporating 10 at% of Cr^{3+}. Magnetic measurements showed an increase in T_N from ~ 42 K for x=0 to ~ 130 K when x reached 0.4. Along with increased in T_N, magnetization reversal with spin reorientation and magnetic switching effect is also observed as x reached 0.3. This type of material can be used in magnetic switching, magneto caloric and spintronics devices.